RSC Applied Polymers

ROYAL SOCIETY OF CHEMISTRY

PAPER

View Article Online
View Journal

Check for updates

Cite this: DOI: 10.1039/d5lp00212e

Controlled *in situ* acidification enables the 3D printability of GelMA–dextran aqueous two-phase hydrogel with unique interconnected porosity

Evdokia Stefanopoulou, *[a,b] Ghazi Ben Messaoud, [c] Rodrigo Salazar Ortiz,[d] Horst Fischer [d] and Walter Richtering *[a,b]

Hydrogels with tailored porosity and microstructure are essential for biomedical applications such as drug delivery and tissue engineering, yet precise control over their internal architecture remains a challenge. A promising strategy relies on bicontinuous systems formed *via* spinodal decomposition of polymer blends, enabling the design of hydrogels with tunable and interconnected porosity. By selectively using one polymer as a sacrificial template, hydrogels with large interconnected pores can be developed, enhancing cell growth and migration, nutrient transport, and cellular waste removal. However, the inherent instability of bicontinuous systems, makes it difficult to arrest the microstructure at a defined stage, limiting reproducibility and precise control over pore architecture. Herein we report a straightforward strategy to regulate the phase separation process of GelMA–dextran aqueous two-phase systems (ATPS), enabling 3D printing of hydrogels with tunable porous microarchitectures. By introducing glucono delta-lactone (GDL) into the ATPS, a gradual decrease in pH is achieved, which delays and slows down the kinetics of phase separation. UV photocrosslinking at a selected time point arrests the evolving bicontinuous structure, offering precise control over the pore size and morphology. The results confirm fine-tuning of the phase separation dynamics and enhanced reproducibility. Notably, the GDL-mediated pH control stabilizes the mixture long enough to allow 3D printing, without interfering with the phase separation or the final microstructure. The printed hydrogels retain their interconnected morphology, with tunable channel sizes depending on the timing of crosslinking. This approach offers a robust and versatile route to structure hydrogels with controlled porosity and architecture. It opens new opportunities for the design of biofunctional materials with improved mass transport and mechanical properties, tailored to specific biomedical applications, and it is compatible with advanced fabrication methods like 3D printing.

Received 11th July 2025,
Accepted 3rd November 2025

DOI: 10.1039/d5lp00212e

rsc.li/rscapplpolym

Open Access Article. Published on 04 November 2025. Downloaded on 12/18/2025 4:14:42 PM.
This article is licensed under a Creative Commons Attribution 3.0 Unported Licence.

1. Introduction

Polymeric hydrogels are three-dimensional networks composed of physically or chemically cross-linked polymers, with a water-retaining capacity and unique architecture that can withstand great mechanical stresses. Hydrogels can be prepared using natural, synthetic polymers, or their mixtures. Synthetic polymers offer great control of gel microstructure, mechanical properties, high load-bearing capacity[1] and degradation rates, while natural polymers offer better biological properties and biocompatibility.[2,3] Due to their versatility, polymeric hydrogels are widely used in different fields, including food,[4] nutraceutical systems,[5] environment and energy applications,[6] pharmaceutical[7] and biomedical applications.[8,9]

Although the mechanical properties, degradation rate and biocompatibility of hydrogels can be tuned through the selection of polymers and gelation conditions, the controlled introduction of macroporosity, beyond the inherent mesh-like structure of polymer networks, remains particularly challenging. In a recent study, the mesh size (effective pore size) of agarose hydrogels was systematically measured in the range of (25–100) nm, by varying the polymer concentration.[10] Another work reports porous hierarchically-ordered hydrogels, where the morphology and size of porosity is dictated by the choice of solvent and the polymer concentration and pore size extends up to 50 μm,[11] which could be restrictive for cell applications. Alternatively, porosity can be introduced into hydrogels with techniques such as templating methods, gas

[a]DWI Leibniz Institute for Interactive Materials, Forckenbeckstrasse 50, 52074 Aachen, Germany. E-mail: stefanopoulou@pc.rwth-aachen.de
[b]Institute of Physical Chemistry, RWTH Aachen University, Landoltweg 2, 52074 Aachen, Germany. E-mail: richtering@pc.rwth-aachen.de
[c]STLO, INRAE, Institut Agro, 65 Rue de Saint-Brieuc, 35042 Rennes, France
[d]Department of Dental Materials and Biomaterials Research, RWTH Aachen University Hospital, Pauwelsstrasse 30, 52074 Aachen, Germany

© 2025 The Author(s). Published by the Royal Society of Chemistry

Open Access Article. Published on 04 November 2025. Downloaded on 12/18/2025 4:14:42 PM.
This article is licensed under a Creative Commons Attribution 3.0 Unported Licence.

injection, electrospinning, freeze-drying, or phase separation, and each of them is targeting a porosity at different length scales.[12,13] Among the commonly used ones, the development of an aqueous two-phase system (ATPS) is a promising approach to introduce porosity, as it occurs in a fully aqueous medium and does not require any specific device. Pores are created within the hydrogel, by inducing gelation of one of the two polymers composing the water-in-water (w/w) emulsion, while the second one is used as a sacrficial template. Control of the kinetics and the mechanism of phase separation enables the creation of hydrogels with porosity sizes that vary from disconnected to interconnected pores, and from unoriented and randomly distributed to highly oriented bands or fibers.[14]

Many recent studies focus on the microarchitecture of the hydrogels and how it can facilitate their intended purposes[15,16] without compromising their mechanical robustness.[17] The selection and tunability of the hydrogel microstructure is crucial for targeting the formation of different tissues,[18] for improvement of vasculogenesis and angiogenesis[19–21] and for efficient spreading and migration of cells and nutrients.[22–25] The optimal range of pore size for the diffusion of nutrients within scaffolds *via* blood vessels should be larger than 30 μm.[26] For cell proliferation, the macroporosity range is targeted: pores of (120–325) μm are reported ideal for osteoblast cells,[27] whereas the range (200–250) μm is more suitable for human dermal fibroblast cells.[28] Additionally, porosity requirements in hydrogels can vary between arrangements of isolated cells and cells that form clusters, like the islets of Langerhans in the pancreas for the regulation of blood glucose level,[29] where interconnected pores are beneficial for proper transport of oxygen and nutrients. A well-defined porosity is also crucial for the diffusivity of drugs in drug delivery systems, enabling the local and timely release of therapeutic agents. For instance, smaller pores sizes reduce the rate of drug release, making it possible to achieve sustained release profiles for chronic treatments, while larger pores sizes facilitate rapid drug delivery for acute scenarios.[17]

In general, liquid–liquid phase separation can be associative (single polymer–salt coacervation, complex coacervation between polymers) or segregative (demixing through ATPS formation), depending on the respective charge-induced or water-affinity interactions. ATPS are mixtures of two thermodynamically incompatible polymers that phase separate and form w/w emulsions. Due to their fully aqueous environment and ultralow interfacial tension, ATPS are widely studied[30–32] and used in numerous bioapplications, ranging from the lubrication of joints[33] to the encapsulation of active biomolecules like DNA.[34] If combined with 3D printing technologies, ATPS can be advantageous for the fabrication of hydrogels with tailorable and hierarchical porosities on the macroscale, mesoscale and microscale *via* a single step,[35,36] or for improving the quality of low-viscosity bioinks.[37]

The choice of (bio)polymers is also significant, both in terms of controlling the segregative phase separation process for ATPS formation and in terms of ensuring biocompatibility. Gelatin methacryloyl (GelMA) is a modified protein that is ideal in both respects, because of its functional ionizable carboxylic and amino groups, RGD (Arg–Gly–Asp) motifs for cell adhesion and proliferation, and matrix metalloproteinase degradation sites for cell remodelling.[38] GelMA is also widely used as a bioink component for 3D printing due to its microrheological, viscoelastic, and shear-thinning properties.[16,24,39,40] On the other hand, dextran is a neutral bioinert polysaccharide.[41] Under specific physicochemical conditions and in absence of attractive interactions, protein–polysaccharide systems are known to be thermodynamically incompatible due to their water affinity difference.[42] Incompatibility is further influenced by changes in temperature, pH, ionic strength of the solution and the molecular weights and concentrations of the used polymers.[43]

Segregative phase separation of a protein and polysaccharide mixture in water can occur by two different mechanisms, namely nucleation and growth, or spinodal decomposition. In the nucleation and growth mechanism, the system is metastable and only concentration fluctuations above a critical size (nuclei) will develop, while the rest will disappear. The size of the formed droplets generally increases with Ostwald ripening, leading to polydisperse droplets of one polymer-rich phase dispersed in the second one. In the absence of quenching, the droplets coalesce until a macroscopic phase separation is achieved with the formation of two distinct phases, each of which is rich in one polymer. In the case of spinodal decomposition, the system is unstable and phase separation develops spontaneously from small local fluctuations in concentration that grow fast over time. Due to the thermodynamic instability and rapid phase separation kinetics of the system, targeting segregative phase separation through spinodal decomposition to develop functional porous hydrogels remains challenging.[32,44]

It has already been shown that, in the case of the GelMA–dextran system, an amphiphlic, amphoteric protein/neutral polysaccharide system, the formation of ATPS is governed by the charge density of GelMA and can be triggered either by adding salts or by decreasing the pH around the isoelectric point (IEP) of GelMA.[22] Phase separation has been triggered so far by manually adjusting the pH of the w/w emulsion, using a small quantity of hydrochloric acid. However, this method has some limitations with regard to controlling the size of the pores of the resulting hydrogels and the time requirements for 3D printing them. Adjusting the molarity of HCl to immediately induce segregation of the GelMA–dextran ATPS requires considerable effort to process the system, by trying to control the competition between phase separation and gelation during 3D printing. In this work, an *in situ* acidification approach of the GelMA–dextran ATPS is proposed, which enables a straightforward and controlled transition from a monophasic to a biphasic GelMA–dextran system. For this, glucono-δ-lactone (GDL) is introduced, which is an organic bio-molecule that derives from the aerobic oxidation of glucose. In an aqueous solution, GDL slowly hydrolyzes to form gluconic acid.[45,46] The hydrolysis process is a first-order reaction and its rate is influ-

© 2025 The Author(s). Published by the Royal Society of Chemistry

Open Access Article. Published on 04 November 2025. Downloaded on 12/18/2025 4:14:42 PM. This article is licensed under a Creative Commons Attribution 3.0 Unported Licence.

enced by several factors, including the concentration of GDL, the temperature and the initial pH of the solution.[47,48] In general, an increase in the GDL concentration, temperature or initial pH accelerates the kinetics of the hydrolysis and, therefore, the decrease in pH.

GDL has been widely used in the food industry as a slow acidifier. GDL is also suitable for the gelation of pH-sensitive systems, including the pH-driven self-assembly of amphiphilic molecules.[49–52] Moreover, due to its biocompatibility and great solubility in water, GDL has applications in tissue engineering, where it enables controlled and homogeneous gelation and the production of mechanically robust scaffolds.[53] Controlled gelation is also essential for 3D printing of hydrogels, where GDL is used to enhance the viscosity of bioinks.[54]

Building on these features, the use of GDL as a versatile agent for slow acidification is investigated, in order to tune the phase behavior of GelMA–dextran mixtures. Specifically, it is demonstrated that the hydrolysis of GDL into gluconic acid offers a controllable alternative to the conventional addition of HCl to initiate phase separation. By adjusting both the concentration of GDL and its hydrolysis kinetics, precise control over the rate and extent of the pH decrease in GelMA–dextran systems is achieved. This tunable *in situ* acidification strategy proves especially advantageous for controlling the onset time of phase separation, specifically in the case of spinodal decomposition, resulting in delayed phase separation of the GelMA–dextran system.

From an application perspective, the addition of GDL would be beneficial for 3D printing, particularly with the inkjet technique, in which the ink must be in liquid state. The introduced delay of phase separation allows sufficient time for setting up the 3D printer and provides the flexibility to create larger and more complex patterns that require longer printing times. Additionally, the size of the resulting microstructure can be controlled by 3D printing at different stages of the phase separation process.

2. Experimental

2.1. Chemicals

Gelatin type-A from porcine skin (LOT # SLCJ2223, molecular weight range (50–100) kDa, corresponding to a bloom strength value of 300 g), phosphate buffered saline (PBS) and NaOH pellets, methacrylic anhydride (MAA), dextran from leuconostoc spp. ((450–650) kDa, LOT # BCCF8905), GDL (M_w = 178.14 g mol^{-1}), photoinitiator 2-hydroxy-4′-(2-hydroxyethoxy)-2-methylpropiophenone (Irgacure 2959, M_w = 224.25 g mol^{-1}) and rhodamine B isothiocyanate (RITC, M_w = 536.08 g mol^{-1}) are supplied by Sigma-Aldrich and are used for the preparation and characterization of hydrogels. In addition, for comparison purposes between the HCl and the GDL acidification techniques, a HCl 1 M stock solution was purchased from VWR. All solutions are prepared in Milli-Q water.

2.2. GelMA synthesis

Methacrylation of native gelatin introduces methacryloyl groups, which enable efficient formation of irreversible hydrogels at 37 °C through UV photo-crosslinking. The methacrylation reaction is performed according to the protocol developed by Lee *et al.*[55] First, gelatin 10% w/v is dissolved in a PBS buffer solution at 60 °C. Then 0.1 mL MAA per 1 g of gelatin is added dropwise to the system, in equal portions, every 30 minutes for 3 hours. The methacrylation reaction takes place under constant stirring at 50 °C and results in the acidification of the solution, which must be continuously monitored and adjusted to neutral pH by adding appropriate amounts of NaOH 5 M. The synthesized GelMA is then purified by dialysis, using a membrane cutoff of (12–14) kDa. The final GelMA foam is obtained after freeze-drying and is stored in the freezer at −20 °C until further use.

2.3. Preparation of mixtures in solution state

GelMA foam is solubilized in Milli-Q water at 60 °C for 30 min, while dextran is soluble at room temperature. Before the preparation the two polymer mixtures in the desired concentrations, all stock solutions are equilibrated at 37 °C for at least 20 min. Two microstructures are targeted: dextran droplets dispersed in the GelMA continuous phase and bicontinuous systems where the channels of each biopolymer are interconnected. The compositions are: for the dextran droplets [GelMA] = 54 mg mL^{-1} and [dextran] = 11 mg mL^{-1} and for the bicontinuous [GelMA] = 54 mg mL^{-1} and [dextran] = 22 mg mL^{-1}.

The specific phase separation conditions-namely concentrations of GelMA, dextran and pH– are dependent on the molecular features of the GelMA and the dextran. In particular, the molecular weight and the distribution of molecular weights of both polymers, as well as the methacrylation degree of GelMA are all important parameters to take into account. In this work, the range of the molecular weight of the used gelatin batch is within the typical ranges and molecular weights of GelMA used in the literature.[56–58] An increased molecular weight of dextran ((1500–2800) kDa) has been explored in preliminary tests, but it had no effect on the phase separation conditions. A decrease in the methacrylation degree of the synthetized GelMA does not significantly affect the isoelectric point (Fig. S1, SI), hence the conditions for phase separation. However, it influences the mechanical properties of the produced hydrogels. Although a lower methacrylation degree means stiffer hydrogels at room temperature, softer and more fragile hydrogels are obtained at an increased temperature (37 °C) and after photocrosslinking of the GelMA phase. The decision for the selected methacrylation degree of GelMA and molecular weight of dextran is based on these error tests.

2.3.1. Manual acidification with HCl. An amount of HCl in the mM range is added to the GelMA–dextran solution, to adjust the pH close to the IEP of GelMA and trigger phase separation. The solution becomes turbid upon addition of HCl, indicating the phenomenon of phase separation. If the pH decreases below the IEP of GelMA by ≈0.9 unit pH, the solution becomes transparent and GelMA is miscible with dextran again.

Open Access Article. Published on 04 November 2025. Downloaded on 12/18/2025 4:14:42 PM. This article is licensed under a Creative Commons Attribution 3.0 Unported Licence.

2.3.2. *In situ* acidification with GDL. The hydrolysis of GDL into gluconic acid is used as an alternative *in situ* acidification of the GelMA–dextran solution. Initially, a monophasic GelMA–dextran aqueous solution is prepared and the weighed GDL powder is dissolved (at $t = 0$). Solubilization of GDL is achieved almost instantaneously after vortexing the solution. The acidification rate of the ATPS depends on the used GDL concentration (0.25, 0.50 or 1.00% w/v). The moment when phase separation starts is named "onset time" in all time-dependent experiments.

2.4. UV-Vis spectroscopy

UV-Vis spectroscopy is employed to monitor the evolution of turbidity in GelMA–dextran mixtures as a function of pH, acidifier concentration and, in the case of GDL, time. Solutions with dextran droplets in the GelMA continuous phase ([GelMA] = 52 mg mL^{-1} and [dextran] = 12 mg mL^{-1}) and bicontinuous ([GelMA] = 54 mg mL^{-1} and [dextran] = 22 mg mL^{-1}) resulting microstructures are investigated. All measurements are performed by the JASCO V-500 spectrophotometer at 37 °C. The scanning wavelength range is (400–700) nm and the absorbance (ABS) at 600 nm is selected as indicative value for the calculation of turbidity = $100 - T(\%)$, where T is the transmittance $T = 10^{-ABS}$.

2.5. Preparation of hydrogels

The fluorescent dye RITC and the photoinitiator Irgacure 2959 (5 mg mL^{-1}) are added to solubilize along with the GelMA foam at 60 °C. The solution is filtered (acrodisc PSF with GXF, 0.45 μm) in order to remove any impurities. The dextran solution is prepared at room temperature, after some vortexing and gentle stirring.

2.5.1. Casting of hydrogels. Mixtures of GelMA–dextran and the selected acidifier are prepared at 37 °C, a small volume is poured into the wells of a 96-multi-well plate and irreversible hydrogels are obtained after (2–4) min of UV exposure (UV LED lamp, 30 W, 365 nm, 14 mW cm^{-2}). By UV-curing, quenching of the microstructure is achieved. From dextran-rich droplets dispersed in a GelMA-rich continuous phase, hydrogels with regular disconnected pores are obtained, after gelling GelMA and washing away dextran. Similarly, from a bicontinuous solution that undergoes spinodal decomposition, hydrogels with interconnected porosity are created, after gelation of the GelMA-rich phase and washing away the dextran-rich solution to create the pores.

2.5.2. Inkjet 3D-printing of hydrogels. Mixtures of GelMA–dextran in Milli-Q water are prepared and are temporarily stored in an incubator at 37 °C. GDL (10 mg mL^{-1}) is weighed separately in an Eppendorf. A CELLINK BIO X bio-printer is used for inkjet 3D printing of the ATPS solution. In this set of experiments, the electromagnetic droplet (EMD) printhead is attached to the bio-printer and both this and the printer's bedding are pre-heated at 37 °C. A microvalve of 600 μm is mounted to the bottom part of the EMD, the air pressure is set to 25 kPa, the printing speed is 10 mm s^{-1}, with an opening time of 5 ms and a cycle time of 250 ms. The GelMA–dextran water mixture is added to the Eppendorf containing the weighed GDL powder, a timer is started ($t = 0$) and the GelMA–dextran–GDL aqueous solution is added to the cartridge which is mounted on the printhead. After parameter input and printhead calibration, printing of the desired pattern begins during phase separation. In this work, 3D printing is performed using a buffer-free solution of GelMA, dextran and GDL, in order to successfully trigger spinodal decomposition. Additional efforts are required to develop the bicontinuous system under physiological conditions. Nonetheless, immediately after printing, the pattern is exposed to UV light to induce photo-crosslinking, thereby arresting the microstructure. Once the structure is fixed, dextran can be immediately removed and cells may be seeded to the hydrogel in physiological conditions.

2.6. Confocal laser scanning microscopy (CLSM)

The Leica SP8 Tandem Confocal System is utilized for *ex situ* or *in situ* morphological characterization of hydrogels or ATPS solutions, respectively. Employing a DPSS laser (λ = 561 nm) the RITC-labeled GelMA-rich phase can be detected. A 10× dry objective is used to capture images at 1024 × 1024 resolution. For the observation of solutions at 37 °C, a heating stage is used for temperature control. Image analysis is performed using Fiji (Fiji is just ImageJ) or the Leica Application Suite X (LAS X) for the 3D reconstructions of z-stacks. Aquami is a software that enables quantitative image analysis of complex multiphasic materials such as bicontinuous materials.[59] Using the scale bar of the obtained image, the software applies appropriate masks for each phase and generates a file with important information on structural features, such as the mean diameter of the channels, *i.e.* their width or thickness. In this work, the distribution of the disconnected pores in GelMA hydrogels or the characteristic length scales of the GelMA or dextran channels in bicontinuous hydrogels are calculated.

2.7. Rheology coupled with UV-curing

A Discovery Hybrid Rheometer (DHR 3, TA Instruments) is coupled with a UV-curing light source and is employed to develop hydrogels from GelMA–dextran aqueous solutions (compositions for both regular disconnected and interconnected pores) by photo-crosslinking the GelMA-rich phase. The measuring geometry consists of a stainless steel upper plate (D = 20 mm) and a lower quartz plate, so that the sample can be irradiated from the bottom. Before the rheological experiments, a calibration of the UV intensity on the surface of the quartz plate is performed by a UV radiometer (CON-TROL-CURE, Silver Line). To monitor gelation, a time sweep is performed for 5 min (F_{ax} = 0.1 N, gap = 0.5 mm, f = 1 Hz, γ = 1% within the linear viscoelastic regime), where the temporal evolution of the storage (G') and loss (G'') moduli is recorded. The UV-curing procedure has been optimized in another study[14] and it is implemented similarly here: after the first minute, for two minutes, at a selected irradiation of 100 mW cm^{-2}. After gelation is completed, which is indicated by G' and G'' reaching a plateau, a frequency sweep is performed within a frequency range of (0.01–100) Hz and at a

© 2025 The Author(s). Published by the Royal Society of Chemistry

Open Access Article. Published on 04 November 2025. Downloaded on 12/18/2025 4:14:42 PM.
This article is licensed under a Creative Commons Attribution 3.0 Unported Licence.

strain γ = 1%. All the rheology experiments presented in this work are conducted at room temperature. After rheological measurements, the hydrogels are carefully retrieved with a plastic spatula and their microstructure is probed by CLSM, as a second step.

3. Results and discussion

3.1. Identification of conditions for triggering phase separation

The segregative phase separation between a protein and a polysaccharide is primarily driven by their potential interactions and their different affinities to the solvent. In the case of GelMA, an amphiphilic and amphoteric protein, and dextran, a neutral polysaccharide, demixing is predominantly influenced by the charge density of GelMA. The hydrolysis of GDL in water leads to the formation of gluconic acid, resulting in a gradual decrease in pH. Consequently, the addition of GDL powder to a GelMA–dextran solution enables the system to reach a pH close to the IEP of GelMA, at which its global net charge is zero. Under these conditions, phase separation becomes thermodynamically favorable. In Fig. 1, the evolution of the electrophoretic mobility of GelMA is plotted as a function of time. A GelMA aqueous solution is prepared and GDL powder is added at t = 0, when hydrolysis into gluconic acid starts. Simultaneously, the pH decrease of the GelMA solution is being measured. For the concentrations of [GelMA] = 54 mg mL^{-1} and [GDL] = 1 mg mL^{-1}, the electrophoretic mobility of GelMA in solution grows until GelMA reaches the state of zero global charge after 120 min and at a pH ~ 4.6, close to the IEP of GelMA (Fig. S1, SI).

A higher concentration of GDL amounts to more gluconic acid leading to a faster decrease in pH and a lower final pH, as depicted in Fig. 2A. Increasing the concentration of GDL further to ≥20 mg ml^{-1} results in immediate phase separation, similar to what is observed with a strong acid (*e.g.* HCl). This is due to the fast hydrolysis of GDL, leading to a sufficient amount of gluconic acid solution to instantly decrease the pH to the value at which phase separation occurs. In this case, the slopes are steeper and the initial pH decrease is more rapid. The final pH value drops to (3.0–3.5), whereas the starting pH is between (4.5–5.0) which is already close to the IEP of GelMA. On the contrary, for [GDL] ≤ 2.5 mg mL^{-1}, the amount of acidifier is so small that the pH can only drop to (4.75–5.00). After a long time (>1 h), the pH ≈ pI of GelMA and phase separation starts. The IEP will not be reached if the concentration of GDL is very low (1.25 mg mL^{-1}) and the buffering effect of GelMA in solution predominates. From Fig. 2A it is understood that there is a specific range of GDL concentrations that is relevant for our purposes in this work and these concentrations

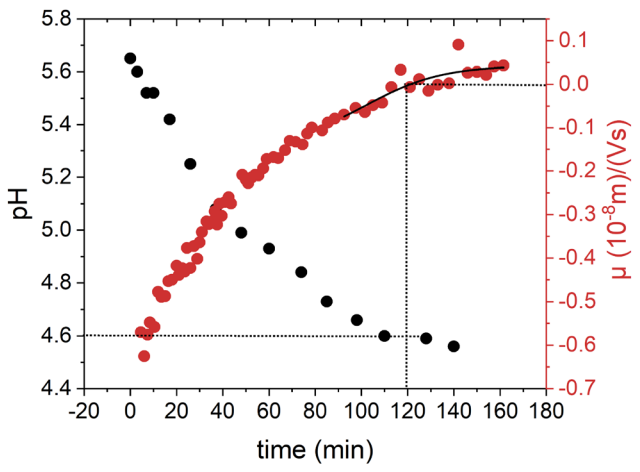

Fig. 1 Temporal evolution of the pH (black) and the electrophoretic mobility of 54 mg mL^{-1} of GelMA (red) after addition of 1 mg mL^{-1} of GDL at 37 °C. After 120 min, the global charge of GelMA reaches zero at pH ~ 4.6.

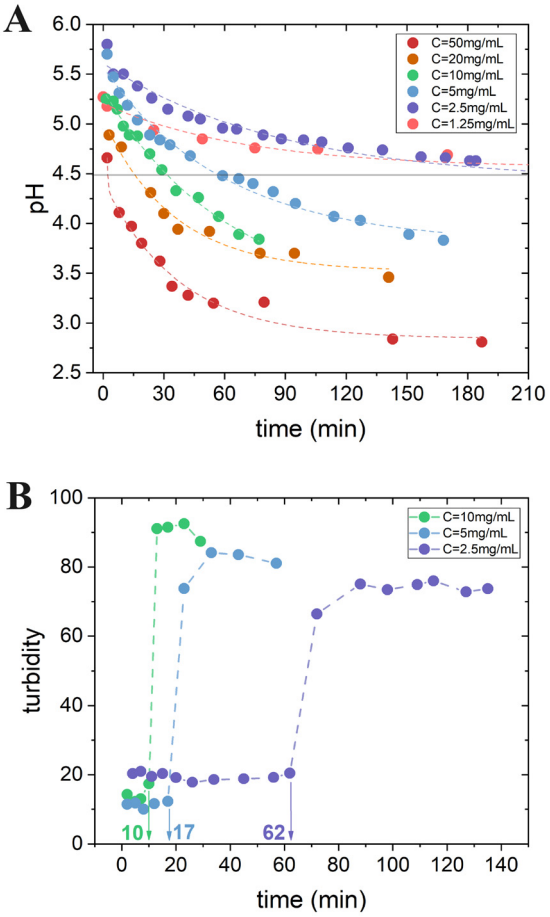

Fig. 2 (A) Temporal evolution of pH for six GelMA–dextran solutions of the same composition and different GDL concentrations at 37 °C. The higher the concentration of GDL, the faster the kinetics of hydrolysis (steeper slope) and the lower the pK_a. (B) Temporal evolution of turbidity increase for three GelMA–dextran solutions of the same composition and different GDL concentrations at 37 °C. The higher the concentration of GDL, the faster the onset of phase separation, as indicated by the sudden increase in turbidity after 10, 17 and 62 min for GDL 1.00% w/v (green), 0.50% w/v (blue) and 0.25% w/v (purple), respectively.

Open Access Article. Published on 04 November 2025. Downloaded on 12/18/2025 4:14:42 PM. This article is licensed under a Creative Commons Attribution 3.0 Unported Licence.

(10, 5 and 2.5 mg mL^{-1}) are further investigated by UV-Vis spectroscopy.

Turbidity measurements provide an indicator of phase separation in GelMA–dextran systems. Although this technique does not distinguish between the mechanisms of phase separation, namely spinodal decomposition and nucleation and growth, it is valuable for identifying the onset of the process. Specifically, turbidity increases when the pH drops sufficiently to reach the IEP of GelMA, where phase separation becomes thermodynamically favorable. In both spinodal decomposition and nucleation and growth, the growing microstructures result in a non-transparent solution due to the light that they scatter. The turbidity values of the selected system of [GelMA] = 54 mg mL^{-1} and [dextran] = 22 mg ml^{-1} as a function of time are measured by UV-Vis spectroscopy and the results are illustrated in Fig. 2B. The arrows indicate the time at which the turbidity of the solution starts to increase, confirming the start of phase separation. The onset time of GelMA–dextran demixing increases with decreasing GDL concentration from 62 to 10 min, for [GDL] = 2.5 mg mL^{-1} and [GDL] = 10 mg mL^{-1}, respectively. This experiment demonstrates how the adjustment of the GDL concentration is a straightforward approach to control the onset time of phase separation.

3.2. Morphological analysis of the GelMA–dextran solutions

The microstructural evolution of the GelMA–dextran w/w emulsion over time and following GDL addition is monitored using CLSM. This technique provides information on the spatial organization of the GelMA-rich and dextran-rich phases, at different time points during the GDL hydrolysis. In Fig. 3, we observe the GelMA–dextran system in solution state, at T = 37 °C. Temperature control is crucial and is achieved using the heating stage of the CLSM, to avoid that GelMA undergoes physical gelation[60,61] through conformational change from random coil to triple helix, which would quench the microstructure.

The system composed of [GelMA] = 54 mg mL^{-1}, [dextran] = 11 mg mL^{-1} and [GDL] = 5 mg mL^{-1} (Fig. 3, first row) has an onset of phase separation at t = 30 min and the microstructure is maintained for at least 1 h at 37 °C. Distinct polysaccharide-rich droplets are dispersed within the protein-rich continuous phase and they grow over time. The average diameter of the droplets, as calculated by the software *Aquami*, is between (10.1–18.6) μm. Spinodal decomposition can be triggered by doubling the concentration of dextran and keeping the rest of the composition the same (Fig. 3, second row). The system is initially monophasic (before 26 min), because the pH of the solution is still far from the IEP of GelMA (starting at pH ≈ 5.5). In the early stage of spinodal decomposition, at 26:30 min from the start of the hydrolysis of GDL, slight fluctuations in concentration of one phase into the other are distinguishable. At 28 min, the bicontinuous microstructure with interwoven elongated channels has grown homogeneously, and at 30 min, the characteristic length scale of the channels is already ≈200 μm in diameter. Shortly after 30 min, the system turns into a multiple emulsion (dextran-in-GelMA-in-

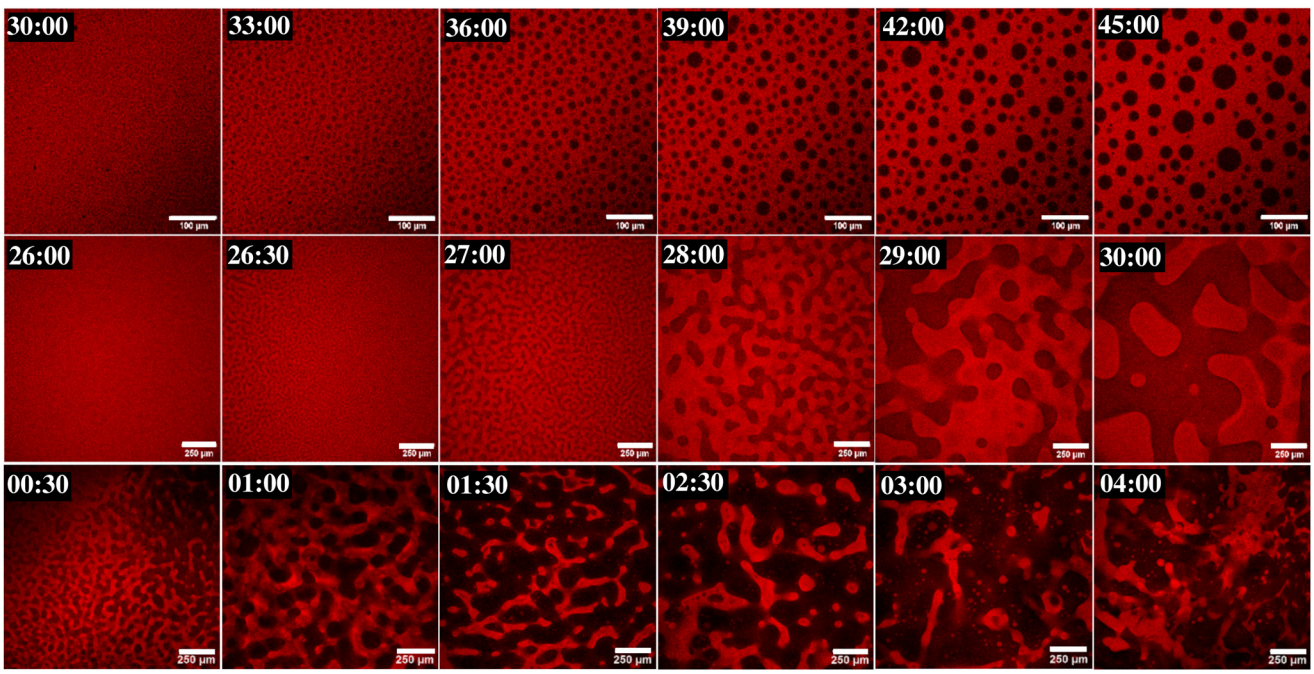

Fig. 3 CLSM images of the GelMA–dextran phase-separating solution at 37 °C. GelMA is labeled red. First row: dextran droplets in the GelMA continuous phase, in presence of GDL, evolution after t = 30 min. Scale bars: 100 μm. Second row: bicontinuous GelMA–dextran channels, in presence of GDL, evolution after t = 26 min. The full evolution of spinodal decomposition takes place within 4 min, with growing interconnected channels. Scale bars: 250 μm. Third row: bicontinuous GelMA–dextran channels, in presence of HCl, growing immediately at t = 0 min. A multiple emulsion is formed already 2 min after the HCl addition and the kinetics of phase separation are faster. Scale bars: 250 μm.

© 2025 The Author(s). Published by the Royal Society of Chemistry

Open Access Article. Published on 04 November 2025. Downloaded on 12/18/2025 4:14:42 PM.
This article is licensed under a Creative Commons Attribution 3.0 Unported Licence.

dextran) and continuously evolves until the point of macroscopic phase separation (not depicted).

In the second row of Fig. 3, phase separation has not reached the stage of equilibrium compositions and a small fraction of GelMA appears in the dextran-rich phase. In segregative phase separation, in all intermediate stages before complete demixing, it is expected that each phase is rich in one polymer but contains some polymer of the second phase. It is known from literature that the RGD (Arg–Gly–Asp) motifs of GelMA contribute to cell adhesion and proliferation, so any GelMA remaining sites in the bicontinuous dextran-rich channels would only provide additional adhesion sites, and would not oppose cell invasion as shown in our previous work.[22] Additionally, after photocrosslinking of the GelMA-rich phase and washing away dextran to create the interconnected porous channels, the GelMA concentration at those sites is so low in the pores that no continuous network can be formed and it they are washed away along with dextran.

Although spinodal decomposition is fast, transient and sensitive to experimental procedures, GDL allows for better control over the onset point of phase separation as well as for a time window of ≈5 min during which the bicontinuous microstructure is maintained. To better demonstrate this point, a direct comparison of the temporal evolution of the bicontinuous GelMA–dextran microstructure due to the HCl-induced acidification is depicted in the third row of Fig. 3. Herein, the interconnected GelMA and dextran channels are immediately formed and remain bicontinuous during the first (1–2) min. Afterward, a multiple emulsion begins to form, where the elongated channels and droplets of the GelMA-rich phase coexist within the continuous dextran-rich phase and *vice versa*, for example, at t = 3 min. In summary, GDL hydrolysis offers an extended "time window" and better control of the kinetics of phase separation compared to HCl-induced acidification, where phase separation is complete in (1–2) min. In addition, GDL allows for precise control over the onset of phase separation, since acidification occurs gradually, unlike the immediate drop in pH with HCl.

The temporal evolution of the diameters of the elongated bicontinuous channels of the GelMA–dextran aqueous solution is obtained by quantitative analysis of the CLSM images. In Fig. 4A, the characteristic length scales of both the GelMA-rich (brown) and dextran-rich (black) regions are growing with time. The grey-outlined region in Fig. 4A is the range of length scales that is desirable for feeding the cells into the interwoven channels. The achieved diameters of the formed channels in the evolution of spinodal decomposition are the widths of the pores that are to be formed after photo-crosslinking the GelMA-rich phase and removing the dextran-rich phase. The length scales of the pores are ideal for the attachment, growth and migration of cells.

The presence of GDL in the GelMA–dextran aqueous solution slows down the kinetics of the otherwise fast-progressing spinodal decomposition. Herein, additional physicochemical conditions –such as temperature, presence of salt ions, and dilution– are assessed as means to further control the evolution of the ATPS. Temperature decrease can slow down the hydrolysis of GDL, therefore decreasing the acidification rate. Salt affects the ionic strength of the starting solution, screening the counterions of GelMA, and has the potential to act as stabilizer of w/w emulsions *via* percolation-to-cluster transitions.[62,63] Dilution of the initial GelMA–dextran–GDL composition reduces the overall concentration of each polymer and can directly affect phase separation kinetics[64] due to increased solvent effects, changes in diffusion distances, and decreased polymer–polymer interactions.

A quantitative analysis of the obtained confocal images for different physicochemical conditions or compositions that lead to spinodal decomposition *via* GDL *in situ* acidification is possible using the software *Aquami*. A similar quantitative ana-

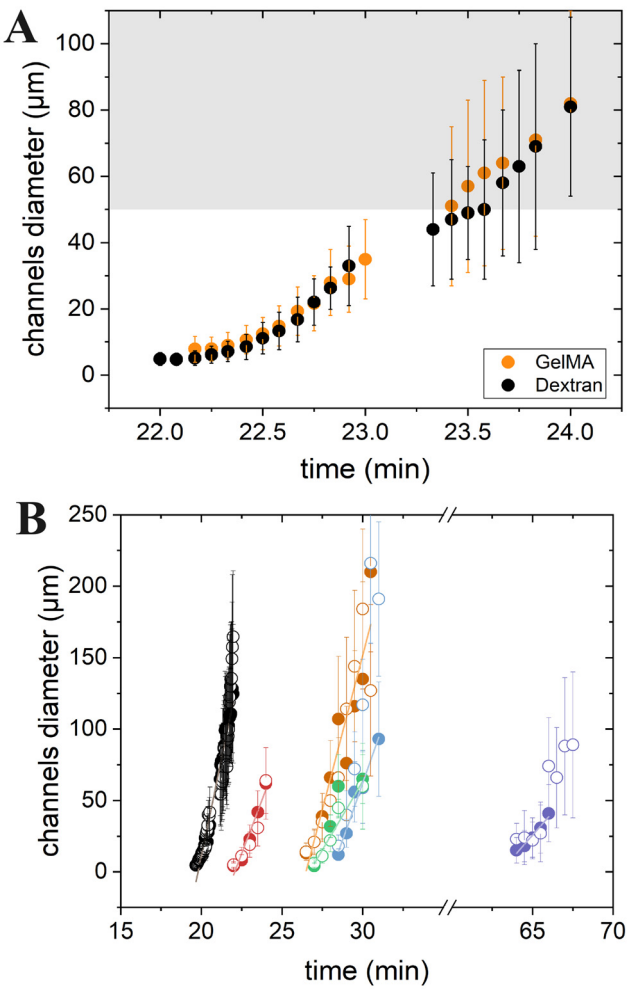

Fig. 4 Temporal evolution of the width of the elongated interwoven channels of GelMA–dextran in solution state, at 37 °C. (A) Characteristic length scales of the channels of GelMA (brown) and dextran (black). Composition: [GelMA] = 54 mg mL^{-1}, [dextran] = 22 mg mL^{-1}, [GDL] = 5 mg mL^{-1} at 37 °C. (B) Characteristic length scales of the channels of GelMA (closed) and dextran (open). Conditions: (4A) composition in black, increased [dextran] = 24 mg mL^{-1} (red), decreased T = 30 °C (orange), 1 mM NaCl addition (green), 1.1× dilution (blue) and decreased [GDL] = 2.5 mg mL^{-1} (purple).

Open Access Article. Published on 04 November 2025. Downloaded on 12/18/2025 4:14:42 PM.
This article is licensed under a Creative Commons Attribution 3.0 Unported Licence.

lysis is not possible for the HCl-induced spinodal decomposition, because in the third row of Fig. 3 it is shown that phase separation starts and finishes much quicker. In Fig. 4B, the varying parameters are the concentration of dextran or GDL in the system, the temperature at which phase separation takes place, ionic strength (1 mM NaCl) and 1.1× dilution of the ATPS. The results will be discussed with respect to the onset time of spinodal decomposition, which depends on the speed of the hydrolysis of GDL and when the pH ≈ pI of GelMA. It is also interesting to compare the slopes of the different sets of data as indicators of the kinetics of spinodal decomposition, as well as the time window from the onset time until the late stage of macroscopic phase separation, at which no further quantitative analysis of the obtained confocal images is possible.

The onset time can be easily tuned by adjusting the GDL concentration, as depicted in Fig. 4B if we compare the first (black) and last (purple) set of data. This is agrees with the data from the turbidity curves in Fig. 2B. However, spinodal decomposition consistently occurs within (5–6) minutes in both cases.

In Fig. 4B, when comparing the first (black) to the second (red) dataset, the dextran concentration changes from 22 to 24 mg mL^{-1}. This does not significantly affect the time window of phase separation, when comparing the first slope (55 ± 3) μm min^{-1} with the second (29 ± 7) μm min^{-1}. Increasing the dextran concentration provides a (2–3) min additional delay to the onset of phase separation. The decrease in temperature (orange dataset) is limited in the range ($T \geq$ 30 °C) due to the physical gelation of GelMA. For the same GelMA–dextran–GDL composition as the first (black) dataset, a 7 min additional delay of the onset time of spinodal decomposition is introduced. The slope shows a decrease to (44 ± 8) μm min^{-1}, suggesting a negligible influence of this small temperature decrease on the kinetics of phase separation.

The effects of the 1.1× dilution of the ATPS (green dataset) and the presence of a small amount of 1 mM NaCl (blue dataset) in the GelMA–dextran–GDL solution are also examined. When compared to the ATPS with no dilution or no salt (black dataset), both have a similar additional delay of (7–8) min. The slope of the diluted ATPS is calculated (21 ± 9) μm min^{-1}, which is much slower than that of the salt-containing ATPS [(57 ± 13) μm min^{-1}]. To conclude, the onset time of spinodal decomposition is adjustable by choosing the appropriate physicochemical conditions and initial composition of the ATPS and, once it starts, there is also a small impact on the kinetics of segregation.

3.3. Rheology and UV-curing for the formation of hydrogels

The rheological properties of the GelMA–dextran hydrogels are also investigated. The *in situ* gelation of the GelMA-rich phase is performed by the UV curing setup that is coupled to the rheometer. Hydrogels with regular disconnected and interconnected pores are obtained. By controlling the time between GDL addition to the ATPS, at t = 0, and the onset time of UV-curing, hydrogels of different porosities are developed. Their microstructure is probed by CLSM after the rheological experiments. In Fig. 5 it can be verified that the evolution of the GelMA–dextran microstructure can be followed by rheology. For a composition of [GelMA] = 54 mg mL^{-1} and [dextran] = 11 mg mL^{-1}, the temporal evolution from homogeneous to disconnected-porous hydrogels is observed. For a composition of [GelMA] = 54 mg mL^{-1} and [dextran] = 22 mg mL^{-1}, the temporal evolution from homogeneous to bicontinuous hydrogels is observed. After 45 min, very large channels with round-shaped GelMA-rich regions are observed in the continuous dextran-rich phase and *vice versa*.

For the rheological characterization of the hydrogels, temporal evolution of G' and G'' is firstly measured at a constant frequency and shear strain within the linear viscoelastic regime (Fig. 5A and C). The gelation of each hydrogel is confirmed by the sudden increase in the viscoelastic moduli, following UV application, and until they reach a plateau that indicates the completion of the gelation step. In the subsequent frequency sweep step (Fig. 5B and D), a storage modulus of G' ~ (2.5–4.3) kPa is quantified for all hydrogels. This indicates that, although there are morphological differences, there is no obvious relationship between the formed microstructure and the viscoelastic properties. Lastly, it should be stressed that it is not possible to perform this experiment with the conventional manual HCl acidification.

3.4. Inkjet 3D printing of hydrogels

Inkjet printing can be employed to 3D print the GelMA hydrogels in complex macroscopic patterns of high resolution. The experiment is performed in the solution state of the phase-separating GelMA–dextran mixture, at 37 °C and a microvalve of 600 μm is selected for the electromagnetic droplet printhead, in order to print larger droplets that simultaneously preserve the microarchitecture.[65] In Fig. 6, 3D printed GelMA–dextran hydrogels are presented, after performing confocal microscopy. Various stages of phase separation are portrayed and casted hydrogels are also included as reference and for comparison purposes. Shearing effects during 3D printing the phase-separating solution are investigated by comparing the photocrosslinked products of the inkjet printer to the casted counterparts that are photocrosslinked at the same time points.

Fig. 6A shows very early stages of spinodal decomposition at t = 6:30 min. In the case of the casted reference, the hydrogel appears to be not phase separated yet (A1) in comparison to the 3D printed one which has just started to phase separate (A2 and A3). Small bicontinuous channels at t = 7:30 min are depicted in Fig. 6B and they grow bigger one minute later in Fig. 6C. Again, the 3D printed hydrogels (B2 and C2) are in a more advanced stage of phase separation compared to the casted hydrogels (B1 and C1), which can probably be attributed to shearing effects while printing the GelMA–dextran phase-separating solution, *i.e.* shear-induced demixing.

The later stages of phase separation, at t = 9:40 min, have been captured in Fig. 6D. There even bigger bicontinuous channels can be discerned in the casted hydrogel (D1) and

© 2025 The Author(s). Published by the Royal Society of Chemistry

Open Access Article. Published on 04 November 2025. Downloaded on 12/18/2025 4:14:42 PM.
This article is licensed under a Creative Commons Attribution 3.0 Unported Licence.

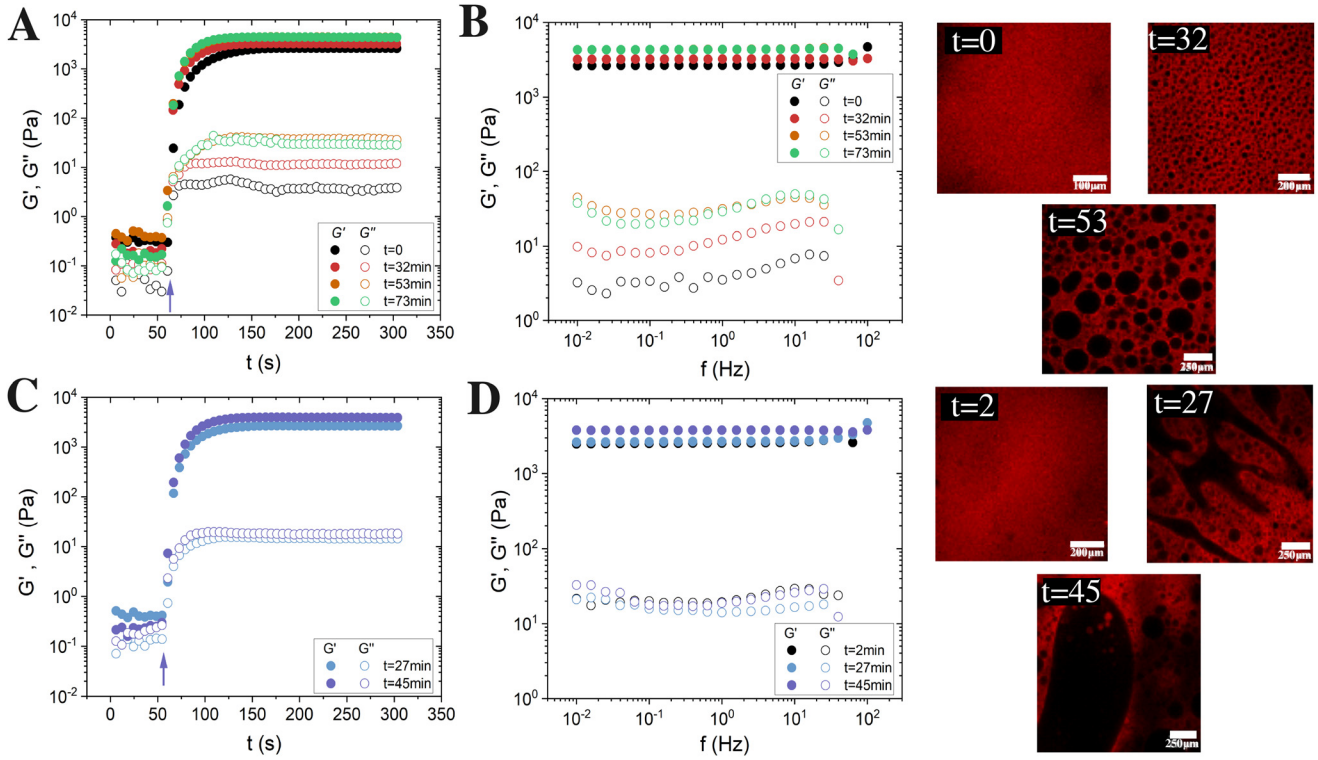

Fig. 5 Temporal evolution of G′ and G″ for 300 s (f = 1 Hz, γ = 1%) for (A) nucleation and growth and (C) spinodal decomposition in presence of GDL. UV-photocrosslinking is performed at different times before or during phase separation, it is indicated by the purple arrows and starts 1 min after loading each GelMA–dextran ATPS onto the rheometer. Frequency sweep f = (0.01–100) Hz at γ = 1% is performed, for hydrogels with (B) regular disconnected and (D) interconnected pores. The obtained microstructure of each hydrogel is probed, as a subsequent step, by CLSM. GelMA is stained red.

also some areas with discontinuity in the 3D printed hydrogel (D2). Lastly, at t = 10:45 min the emulsion transitions to GelMA-rich droplets in the dextran-rich continuous phase (Fig. 6E). In both the casted reference (E1) and the 3D printed droplets (E2), more dextran-rich sites than before are visible. However, the dextran-rich areas of the obtained hydrogels are going to be washed away in the final step, leaving empty spaces (pores) in these places. Therefore, in the case of the last 3D printed droplets, discontinuous and not self-standing hydrogels are produced.

While similar macroscopic patterns as shown in Fig. 6 could, in principle, be produced using a simple syringe-based approach, inkjet-based 3D printing offers several key advantages beyond pattern formation. It provides non-contact material deposition, minimizing disturbance of the ATPS and allowing for rapid, automated fabrication of complex patterns. Specifically, it enables precise, computer-controlled deposition of pico- to nano-liter scale droplets, allowing for high spatial resolution and reproducibility that are difficult to achieve manually. Furthermore, the ability to control the opening time of the microvalves, the printing pressure, the shear stress and the material flow enables the generation of droplets with different volumes within the same construct, providing another level of precision, reproducibility and versatility in material deposition. Especially since the two-phase system is a sensitive material, it requires well-defined conditions during synthesis and processing. Therefore, the adjustment of the interconnectivity of the droplets is achieved by controlling the cycle time of the microvalve, offering the flexibility to print them either individually or continuously as interconnected strands, as shown in confocal micrographs B3 and C3 of Fig. 6.

The inkjet printing experiment successfully illustrates that 3D printing is aided by the addition of GDL to GelMA–dextran ATPS. GDL gradually controls the pH and, because of that, the progression of phase separation. In this way, hydrogels of distinct microporosities can be produced (Fig. S6, SI) and the printed macroscopic patterns can be of high precision and more complex than the casted counterparts. Although the used microvalve has a relatively large diameter of 600 μm, the big droplets that are deposited on the printing surface enable the preservation of the microarchitecture without compromising the shape of the macroscopic 3D printed patterns. A microvalve of a smaller diameter would not be necessary or advantageous in our case, since the targeted length scales of the microstructure are smaller than 250 μm. In this work, inkjet 3D printing is presented as a proof of principle and the printing of more complex structures is an ongoing work. The precise influence of shear forces on the phase separation process remains an important subject for future investigation.

© 2025 The Author(s). Published by the Royal Society of Chemistry

Open Access Article. Published on 04 November 2025. Downloaded on 12/18/2025 4:14:42 PM.
This article is licensed under a Creative Commons Attribution 3.0 Unported Licence.

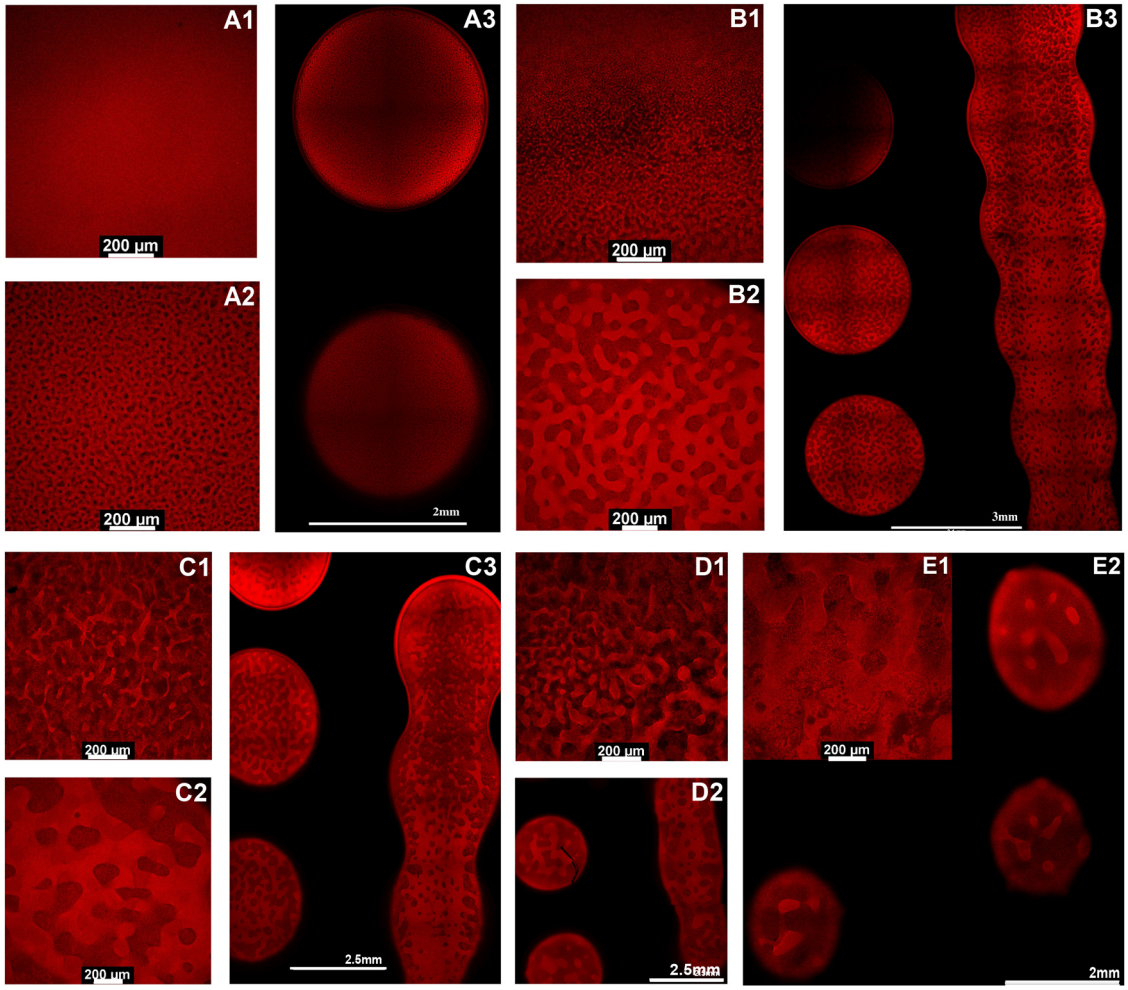

Fig. 6 CLSM images of the casted and 3D printed GelMA–dextran hydrogels photo-crosslinked at different times: (A) very early stages of spinodal decomposition at t = 6:30 min. (A1) Casted reference hydrogel, (A2) and (A3) 3D printed droplets of the hydrogel. (B) Small bicontinuous channels at t = 7:30 min. (B1) Casted reference hydrogel, (B2) and (B3) 3D printed hydrogel. (C) Bigger bicontinuous channels at t = 8:45 min. (C1) Casted reference hydrogel, (C2) and (C3) 3D printed hydrogel. (D) Even bigger bicontinuous channels and some discontinuity at t = 9:40 min. (D1) Casted reference hydrogel, (D2) 3D printed hydrogel. (E) Phase inversion and not self-standing hydrogels at t = 10:45 min. (E1) Casted reference hydrogel, (E2) 3D printed hydrogel.

Additionally, alternative routes to trigger the GelMA–dextran phase separation under physiological conditions are currently being explored, so that the bioprinting of cell-laden structures is possible.

4. Conclusions

This work presents a straightforward strategy to delay phase separation in GelMA–dextran systems, enabling controlled demixing at specific time points after preparation of the solution. The proposed *in situ* acidification *via* addition of GDL allows the adjustment of the onset of spinodal decomposition in a reproducible way. This delayed phase separation opens new possibilities for processing the ATPS, particularly in inkjet 3D printing, where temporal control over demixing is crucial.

The gradual decrease in pH resulting from the hydrolysis of GDL into gluconic acid enables a uniform evolution of microscopic patterns throughout the GelMA–dextran solution. As the pH approaches the IEP of GelMA, a well-defined bicontinuous microstructure is formed. At a chosen time point during this phase separation process, UV crosslinking is used to quench the GelMA-rich domains, while the dextran-rich phase can subsequently be removed, resulting in a porous, interconnected network.

Compared to the abrupt and highly localized pH drop induced by manual HCl addition, where acidification occurs almost instantly (<1 min) and is sensitive to handling and experimental conditions, the GDL-based approach offers a more gradual and controllable acidification process. The acidification rate can be fine-tuned by adjusting the concentration of GDL, *i.e.*, a higher GDL concentration or a shift in physicochemical conditions (temperature, initial pH, and ionic strength). Optimal concentrations that facilitate 3D printing lie

© 2025 The Author(s). Published by the Royal Society of Chemistry

Open Access Article. Published on 04 November 2025. Downloaded on 12/18/2025 4:14:42 PM. This article is licensed under a Creative Commons Attribution 3.0 Unported Licence.

between 2.5 and 10 mg mL^{-1}, corresponding to a delay time of 60 to 10 minutes, respectively. At very low concentrations of GDL, the buffering capacity of GelMA slows acidification, while excessively high concentrations of GDL lead to instantaneous phase separation similar to the manual acidification method using HCl.

The *in situ* acidification approach enables the formation of hydrogels with tunable porosity and characteristic length scales, making it highly relevant for tissue engineering applications. By adjusting the size of porosity, this method can accommodate phenotypically distinct cell types with varying dimensions or cells forming clusters and islets.[29] The proposed method also enables real-time observation of the evolution of the microstructure in the GelMA–dextran aqueous solution, either alone or in the presence of cells and other biomolecules that could be introduced into the segregating system. Such efforts are beyond the scope of this study, and the presented results serve as a proof of principle; however, they provide a valuable foundation for the further optimization of phase-separating bioinks used in 3D bioprinting. Slowing down the phase separation process could also facilitate additional fundamental studies, potentially offering new insights into the demixing mechanisms of protein-neutral polysaccharide mixtures.

The quantitative analysis of the evolution of the microstructure with time confirms that the delay can be easily adjusted by varying the composition (GelMA–dextran–GDL), temperature or ionic strength of the ATPS. The speed of GDL hydrolysis is not severely affected by these variations. The resulting hydrogels exhibit similar mechanical properties regardless of their microporosity, and the measured shear moduli after UV-induced gelation of the GelMA-rich phase show only minor differences.

This study provides an impactful new tool for 3D printing. The GDL addition to the GelMA–dextran mixture successfully aids the inkjet 3D printing in solution state. The introduced delay enables setting up the printer and also provides an optimized time window of controlled pH decrease and phase separation. The 3D printed pattern of the solution can be complex and precise, while the bicontinuous microstructure is also preserved. The ATPS is quenched by UV light at different stages of spinodal decomposition and after 3D printing and GelMA-based hydrogels with unique interconnected pores of different characteristic length scales are obtained. In a broader sense, these findings suggest that the composition of phase-separating bioniks is closely linked to the processing behavior and application potential of hydrogels.

Conflicts of interest

There are no conflicts to declare.

Data availability

Data for this article, including raw files from the different experiments and resulting files from the software *Aquami* for image analysis are available at *Zenodo* at DOI: 10.5281/zenodo.17397768.

Supplementary information (SI) is available and includes information on the isoelectric point of GelMA, phase diagrams, comparison of hydrochloric to gluconic acid, reproducibility tests and some additional macroscopic images of hydrogels after inkjet 3D printing. See DOI: https://doi.org/10.1039/d5lp00212e.

Acknowledgements

This work is funded by the Deutsche Forschungsgemeinschaft (DFG, RI 560/28-1 and FI 975/38-1, project number 516822371).

References

1 H. Yuan, X. Zhao, W. Zhao, Y. Zhang, Q. Ye, S. Liu, B. Yu, S. Ma and F. Zhou, *Adv. Funct. Mater.*, 2025, **35**, 2416898.
2 Y. S. Zhang and A. Khademhosseini, *Science*, 2017, **356**, 3627.
3 Z. Terzopoulou, A. Zamboulis, I. Koumentakou, G. Michailidou, M. J. Noordam and D. N. Bikiaris, *Biomacromolecules*, 2022, **23**, 1841–1863.
4 A. Manzoor, A. H. Dar, V. K. Pandey, R. Shams, S. Khan, P. S. Panesar, J. F. Kennedy, U. Fayaz and S. A. Khan, *Int. J. Biol. Macromol.*, 2022, **213**, 987–1006.
5 D. J. McClements, *Food Hydrocolloids*, 2017, **68**, 238–245.
6 L. Li, P. Wu, F. Yu and J. Ma, *J. Mater. Chem. A*, 2022, **10**, 9215–9247.
7 H. Shoukat, K. Buksh, S. Noreen, F. Pervaiz and I. Maqbool, *Ther. Delivery*, 2021, **12**, 375–396.
8 S. Correa, A. K. Grosskopf, H. Lopez Hernandez, D. Chan, A. C. Yu, L. M. Stapleton and E. A. Appel, *Chem. Rev.*, 2021, **121**, 11385–11457.
9 K. Gul, R.-Y. Gan, C.-X. Sun, G. Jiao, D.-T. Wu, H.-B. Li, A. Kenaan, H. Corke and Y.-P. Fang, *Crit. Rev. Food Sci. Nutr.*, 2022, **62**, 3817–3832.
10 N. L. Cuccia, S. Pothineni, B. Wu, J. Méndez Harper and J. C. Burton, *Proc. Natl. Acad. Sci. U. S. A.*, 2020, **117**, 11247–11256.
11 E. C. Lloyd, S. Dhakal, S. Amini, R. Alhasan, P. Fratzl, D. R. Tree, S. Morozova and R. J. Hickey, *Nat. Commun.*, 2025, **16**, 3792.
12 N. Annabi, J. W. Nichol, X. Zhong, C. Ji, S. Koshy, A. Khademhosseini and F. Dehghani, *Tissue Eng., Part B*, 2010, **16**, 371–383.
13 R. Foudazi, R. Zowada, I. Manas-Zloczower and D. L. Feke, *Langmuir*, 2023, **39**, 2092–2111.
14 G. Ben Messaoud, E. Stefanopoulou, M. Wachendörfer, S. Aveic, H. Fischer and W. Richtering, *Soft Matter*, 2024, **20**, 773–787.

Open Access Article. Published on 04 November 2025. Downloaded on 12/18/2025 4:14:42 PM. This article is licensed under a Creative Commons Attribution 3.0 Unported Licence.

15 Y. Guo, L. S. de Vasconcelos, N. Manohar, J. Geng, K. P. Johnston and G. Yu, *Angew. Chem., Int. Ed.*, 2022, **61**, e202114074.
16 Y. Gu, Y. Zou, Y. Huang, R. Liang, Y. Wu, Y. Hu, Y. Hong, X. Zhang, Y.-C. Toh, H. Ouyang, *et al.*, *Biofabrication*, 2023, **16**, 015003.
17 E. Baur, M. Hirsch and E. Amstad, *Adv. Mater. Technol.*, 2023, **8**, 2201763.
18 E. C. González-Díaz and S. Varghese, *Gels*, 2016, **2**, 20.
19 F. Vanlauwe, C. Dermaux, S. Shamieva, S. Vermeiren, S. Van Vlierberghe and P. Blondeel, *Front. Bioeng. Biotechnol.*, 2024, **12**, 1452477.
20 Y. Luo, T. Zhang and X. Lin, *Chem. Eng. J.*, 2022, **430**, 132926.
21 D. Lu, Z. Zeng, Z. Geng, C. Guo, D. Pei, J. Zhang and S. Yu, *Biomed. Mater.*, 2022, **17**, 025006.
22 G. Ben Messaoud, S. Aveic, M. Wachendoerfer, H. Fischer and W. Richtering, *Small*, 2023, **19**, 2208089.
23 A. Hori, M. Hirata, R. Nonogaki, R. Utoh and M. Yamada, *ACS Omega*, 2025, **10**, 11900–11910.
24 A. J. Seymour, S. Shin and S. C. Heilshorn, *Adv. Healthcare Mater.*, 2021, **10**, 2100644.
25 N. Sengokmen-Ozsoz, M. Aleemardani, M. Palanca, A. Hann, G. C. Reilly, E. Dall'Ara and F. Claeyssens, *Biofabrication*, 2024, **17**, 015012.
26 O. Oliviero, M. Ventre and P. A. Netti, *Acta Biomater.*, 2012, **8**, 3294–3301.
27 C. M. Murphy, M. G. Haugh and F. J. O'brien, *Biomaterials*, 2010, **31**, 461–466.
28 B. B. Mandal and S. C. Kundu, *Biomaterials*, 2009, **30**, 2956–2965.
29 G. Marchioli, L. van Gurp, P. Van Krieken, D. Stamatialis, M. Engelse, C. Van Blitterswijk, M. Karperien, E. de Koning, J. Alblas, L. Moroni, *et al.*, *Biofabrication*, 2015, **7**, 025009.
30 J. Esquena, *Curr. Opin. Food Sci.*, 2023, **51**, 101010.
31 E. Lee, Y. Jo, Y. Kim, H. Yoon, S. Choi, B. Q. Kim, S. Kim and K. Kim, *Mater. Horiz.*, 2025, **12**, 2298–2308.
32 S. Yang, Z. Wang, Y. Meng and X. Wang, *Colloids Surf., A*, 2025, **704**, 135464.
33 Y. Wang, J. Yuan, Y. Zhao, L. Wang, L. Guo, L. Feng, J. Cui, S. Dong, S. Wan, W. Liu, *et al.*, *CCS Chem.*, 2022, **4**, 2102–2114.
34 Y. Wang, J. Yuan, S. Dong and J. Hao, *Langmuir*, 2022, **38**, 4713–4721.
35 F. Chen, X. Li, Y. Yu, Q. Li, H. Lin, L. Xu and H. C. Shum, *Nat. Commun.*, 2023, **14**, 2793.
36 M. Becker, F. Gomes, I. Porsul and J. Leijten, *Biofabrication*, 2025, **17**, 025027.
37 M. Becker, M. Gurian, M. Schot and J. Leijten, *Adv. Sci.*, 2023, **10**, 2204609.
38 J. W. Nichol, S. T. Koshy, H. Bae, C. M. Hwang, S. Yamanlar and A. Khademhosseini, *Biomaterials*, 2010, **31**, 5536–5544.
39 S. Das, J. T. Jegadeesan and B. Basu, *Biomacromolecules*, 2024, **25**, 2156–2221.
40 M. L. Bedell, A. L. Torres, K. J. Hogan, Z. Wang, B. Wang, A. J. Melchiorri, K. J. Grande-Allen and A. G. Mikos, *Biofabrication*, 2022, **14**, 045012.
41 A. Luanda and V. Badalamoole, *Int. J. Biol. Macromol.*, 2023, **228**, 794–807.
42 X. Yang, A. Li, D. Li, Y. Guo and L. Sun, *Trends Food Sci. Technol.*, 2021, **109**, 197–210.
43 X. T. Le, L.-E. Rioux and S. L. Turgeon, *Adv. Colloid Interface Sci.*, 2017, **239**, 127–135.
44 G. Ying, N. Jiang, C. Parra-Cantu, G. Tang, J. Zhang, H. Wang, S. Chen, N.-P. Huang, J. Xie and Y. S. Zhang, *Adv. Funct. Mater.*, 2020, **30**, 2003740.
45 R. A. Lewis, *Hawley's condensed chemical dictionary*, John Wiley & Sons, 2016.
46 Y. Pocker and E. Green, *J. Am. Chem. Soc.*, 1973, **95**, 113–119.
47 D. T. Sawyer and J. B. Bagger, *J. Am. Chem. Soc.*, 1959, **81**, 5302–5306.
48 E. Skou and T. Jacobsen, *Acta Chem. Scand.*, 1982, **302**, 0680250.
49 D. J. Adams, M. F. Butler, W. J. Frith, M. Kirkland, L. Mullen and P. Sanderson, *Soft Matter*, 2009, **5**, 1856–1862.
50 G. Ben Messaoud, P. Le Griel, D. Hermida-Merino, S. L. K. W. Roelants, W. Soetaert, C. V. Stevens and N. Baccile, *Chem. Mater.*, 2019, **31**, 4817–4830.
51 G. Ben Messaoud, P. Le Griel, D. Hermida-Merino and N. Baccile, *Soft Matter*, 2020, **16**, 2540–2551.
52 X. Song, S. He, J. Zheng, S. Yang, Q. Li and Y. Zhang, *Molecules*, 2023, **28**, 3334.
53 H. Yan, D. Huang, X. Chen, H. Liu, Y. Feng, Z. Zhao, Z. Dai, X. Zhang and Q. Lin, *Polym. Bull.*, 2018, **75**, 985–1000.
54 S. Liu, Y. Hu, J. Zhang, S. Bao, L. Xian, X. Dong, W. Zheng, Y. Li, H. Gao and W. Zhou, *Macromol. Mater. Eng.*, 2019, **304**, 1800698.
55 B. H. Lee, H. Shirahama, N.-J. Cho and L. P. Tan, *RSC Adv.*, 2015, **5**, 106094–106097.
56 G.-L. Ying, N. Jiang, S. Maharjan, Y.-X. Yin, R.-R. Chai, X. Cao, J.-Z. Yang, A. K. Miri, S. Hassan and Y. S. Zhang, *Adv. Mater.*, 2018, **30**, 1805460.
57 S. Yi, Q. Liu, Z. Luo, J. J. He, H.-L. Ma, W. Li, D. Wang, C. Zhou, C. E. Garciamendez, L. Hou, *et al.*, *Small*, 2022, **18**, 2106357.
58 E. Walejewska, F. P. Melchels, A. Paradiso, A. McCormack, K. Szlazak, A. Olszewska, M. Srebrzynski and W. Swieszkowski, *Biomacromolecules*, 2023, **25**, 188–199.
59 J. Stuckner, K. Frei, I. McCue, M. J. Demkowicz and M. Murayama, *Comput. Mater. Sci.*, 2017, **139**, 320–329.
60 H. B. Bohidar and S. S. Jena, *J. Chem. Phys.*, 1993, **98**, 8970–8977.
61 M. Djabourov, *Contemp. Phys.*, 1988, **29**, 273–297.
62 M. Vis, V. F. Peters, E. M. Blokhuis, H. N. Lekkerkerker, B. H. Erné and R. H. Tromp, *Phys. Rev. Lett.*, 2015, **115**, 078303.
63 M. Vis, V. F. Peters, E. M. Blokhuis, H. N. Lekkerkerker, B. H. Erne and R. H. Tromp, *Macromolecules*, 2015, **48**, 7335–7345.
64 P. Van de Witte, P. Dijkstra, J. Van den Berg and J. Feijen, *J. Membr. Sci.*, 1996, **117**, 1–31.
65 B. R. Maciel, A. Grimm, C. Oelschlaeger, U. Schepers and N. Willenbacher, *Biofabrication*, 2023, **15**, 045013.

© 2025 The Author(s). Published by the Royal Society of Chemistry